Results in Engineering 27 (2025) 106445

Contents lists available at ScienceDirect

Results in Engineering

journal homepage: www.sciencedirect.com/journal/results-in-engineering

Research paper

Fluid-Dynamic and Structural Optimization of a Suction-Enabled Autonomous Grass-Cutter Robot

Shenoy Adithya Kamalaksha [a], Abhishek Kumar [a], Rithvik Marneni [a], Kamarul Arifin Ahmad [b,c], Spoorthi Singh [a,*], Sharul Sham Dol [d,*]

[a] Mechatronics Department, Manipal Institute of Technology, Manipal Academy of Higher Education, Manipal, Karnataka 576104, India
[b] Aerospace Dept. Faculty of Engineering, University Putra Malaysia, UPM-Malaysia, Serdang 43300, Malaysia
[c] Mathematics Research Institute, University Putra Malaysia, Selangor 43300, Malaysia
[d] Mechanical And Industrial Engineering Department, Abu Dhabi University, Abu Dhabi 59911, United Arab Emirates

ARTICLE INFO

Keywords:
Turbulent duct flow
Reynolds number
Pressure drop analysis
Darcy–Weisbach modelling
CFD validation
Agricultural robotics

ABSTRACT

Autonomous grass-cutter robots are increasingly important for precision agriculture and turf management, offering the potential to reduce labour costs, improve safety, and enhance operational efficiency. However, existing design studies typically address individual subsystems in isolation, lacking a unified framework for comparative evaluation of multi-wheel configurations. To fill this gap, this work introduces a novel, multi-domain integration framework combining structural finite-element analysis (FEA), computational fluid dynamics (CFD) with analytical ΔP–Q and Reynolds number modelling, URDF-based Webots simulation, and Python-driven parametric studies, a unified approach not found in prior grass-cutter robot studies. Key highlights of the paper include: structural optimization, an aluminium 6061-T6 backbone with acrylic panels delivers a 15 % mass reduction while maintaining a safety factor $\geq$ 2.0 under peak loads; suction performance, comparative CFD and Darcy–Weisbach analyses of duct geometries identify the S-type as optimal, with a validated pressure drop of ~0.85 kPa and turbulent intensity ~3.8 % promoting effective debris entrainment; mobility assessment, Webots simulations reveal that a six-wheel chassis enhances traction by 18 % but incurs 12 % higher rolling resistance relative to a four-wheel variant. Analytical modelling modules estimate grass-cutting power, battery endurance (with Peukert's correction), and terrain sensitivity, enabling rapid design optimization. The inclusion of both simulation and fluid-theoretic validation, including Reynolds number, Darcy–Weisbach analysis, and turbulence intensity estimation, offers a robust methodology for optimizing suction flow performance. This integration not only strengthens mechanical and aerodynamic validation but also supports the sustainable development of closed-loop, compost-capable autonomous grass-cutting platforms.

1. Introduction

Autonomous grass-cutter robots have emerged as key enablers in precision agriculture and turf management, offering significant reductions in labour requirements and improvements in operational consistency. Early designs focused on basic rotary-blade implementations, demonstrating that shear-based cutting can be achieved with carbon or stainless-steel blades, achieving effective grass severance through impact and shearing stress [1]. Subsequent work has examined coverage-path planning algorithms tailored for agricultural vehicles to ensure full field traversal with minimal overlap, thereby maximizing energy efficiency and reducing soil compaction [2]. Control strategies for four-wheeled platforms have also been developed, addressing longitudinal and lateral stability in uneven terrain [3], while more recent efforts have leveraged mobile applications for teleoperation and autonomous waypoint navigation in Android-controlled mowers [4]. Chassis design and mobility are critical for reliable outdoor operation. Multi-wheel configurations improve traction and obstacle negotiation: an eight-wheel agricultural robot achieved superior hill-climbing performance through optimized traction allocation [5], and reviews of rolling robots highlight design principles for overcoming obstacles such as stones and ruts [6]. Structural finite-element analyses on light-weight aluminium 6061-T6 chassis frames have demonstrated up to 20 % mass reduction without compromising safety factors, guiding the selection of hybrid aluminium–acrylic backbones for robust yet lightweight designs

* Corresponding authors.
E-mail addresses: spoorthi.shekar@manipal.edu (S. Singh), sharulshambin.dol@adu.ac.ae (S.S. Dol).

https://doi.org/10.1016/j.rineng.2025.106445
Received 12 June 2025; Received in revised form 13 July 2025; Accepted 23 July 2025
Available online 25 July 2025

Nomenclature

Re	– Reynolds number
ΔP	– Pressure drop (Pa)
Q	– Volumetric flow rate (m^3/s)
f	– Friction factor (dimensionless)
L, D	– Duct length and diameter (m)
μ	– Dynamic viscosity of air (Pa·s)
ρ	– Density of air (kg/m^3)
v	– Flow velocity (m/s)
SF	– Safety factor
k	– Peukert's exponent (dimensionless)
C	– Battery capacity (Ah)
t	– Battery discharge time (hours)
τ_s	– Shear strength of grass (Pa)
OCR	– Oxygen Consumption Rate (L/min)
ODR	– Overall Discomfort Rating
WHR	– Working Heart Rate (bpm)
BPDS	– Body Part Discomfort Score
FE	– Field Efficiency (%)
FC	– Field Capacity (ha/h)
SoC	– State of Charge (%)

[7].

Effective debris collection further distinguishes high-performance mowers. Computational fluid-dynamics studies of drum-type forage mowers have mapped airflow fields for optimal plant lifting and feeding, revealing peak gathering and feeding velocities that directly impact cut quality [8]. Self-cleaning multi-stage duct geometries have also been evaluated, showing that tailored curvature and minor-loss profiles reduce clogging and maintain suction efficiency [9]. These findings are underpinned by classical Darcy–Weisbach and continuity relations, which serve as "back-of-envelope" checks on pressure-drop versus flow-rate performance [10]. Robust validation requires both realistic simulation and parametric modelling. The Webots simulator provides a unified URDF-based environment for virtual testing of sensor and actuator models, enabling direct transfer of controllers between simulated and physical robots [11]. Complementary Python frameworks facilitate rapid performance sweeps, varying blade RPM, battery load profiles (incorporating Peukert's correction), and suction parameters, to generate comprehensive performance envelopes directly in Google Colab [12].

Autonomous grass-cutter robots are essential for modern turf and small-scale agricultural operations because they promise to reduce labour requirements, improve cutting consistency, and support sustainable land management. However, existing studies typically focus on single aspects, such as chassis design, debris-collection ducts, navigation strategies, or power management, without examining how these subsystems interact in a complete platform. "While suction systems are common in domestic and agricultural robots, rigorous fluid-dynamic design studies remain scarce. Lai *et al.* (2011) [13] applied CFD with a k–ε model and PRISO algorithm to a vacuum-cleaner duct, demonstrating significant pressure-drop reduction post-optimization. More recently, IET-published work on sweeping vehicles employed response-surface CFD techniques to match nozzle and duct parameters for enhanced suction efficiency. In agriculture, MDPI's [14] CFD-based sprayer study showed that airflow duct geometry substantially affects deposition and flow characteristics. These precedents underscore the value of combining CFD with analytical modelling, a gap our work fills by integrating Reynolds-number-based theory, Darcy–Weisbach loss estimation, and turbulence-intensity characterization into the response duct analysis of our autonomous grass-cutter robot." [15] This siloed approach makes it difficult to understand the trade-offs between vehicle mass, traction, suction efficiency, and battery life that ultimately determine field performance and operational endurance. Recent advancements in IoT-based smart agriculture have demonstrated the impact of embedded systems and fuzzy logic in achieving sustainability through intelligent field automation. Morchid et al. [16] proposed a fuzzy logic–based irrigation system that leverages IoT sensors and cloud computing to optimize water usage, achieving improved soil humidity control and resource efficiency. Their follow-up work [17] presented an embedded, real-time smart irrigation controller using Arduino and multiple soil and environmental sensors, showcasing practical deployment of autonomous irrigation logic. Additionally, Morchid et al. developed a cloud-enabled irrigation system [18] for remote monitoring, while also exploring embedded deep-learning systems for plant disease detection [19] and wildfire alerts in agricultural zones [20]. These studies illustrate how smart control, real-time decision-making, and embedded sensing systems can enhance sustainability in agriculture. While our work emphasizes mechanical and fluid-dynamic optimization of an autonomous grass-cutting robot, these IoT-based contributions provide a complementary foundation for future integration of sensor-based feedback, autonomous operation, and smart compost-cycle control. This study expands existing design efforts by systematically integrating fluid-mechanics-informed suction optimization with structural and mobility validation, creating a holistic evaluation platform for grass-cutting agricultural robots. This fragmented approach limits system-level optimization and prevents comprehensive understanding of trade-offs between structural design, fluid-dynamic performance, mobility under terrain variations, and energy endurance, areas that are inherently interdependent in field robots.

To address these gaps, the present work introduces a unified multiphysics methodology that integrates structural finite-element analysis to optimize a lightweight aluminium-acrylic frame, computational fluid dynamics coupled with Darcy–Weisbach modelling to identify an S-type suction duct, URDF-based Webots simulation to compare four-wheel and six-wheel mobility under stone-ingress scenarios, and parametric Python modules in Google Colab for rapid power, torque, and energy sweeps. This is the first comparative evaluation that holds cutting and suction hardware constant while isolating the impact of wheel count on traction, rolling resistance, and obstacle negotiation. Despite these advances, existing studies treat structural integrity, fluidic suction, mobility, and energy systems in isolation. A unified comparative evaluation of four-wheel versus six-wheel grass-cutter robots, integrating FEA, CFD, Webots simulation, and analytical modelling, remains unexplored. The present work addresses this gap by proposing an end-to-end methodology that quantifies trade-offs in mass, traction, debris-handling, and energy consumption between the two configurations. Beyond mere grass trimming, the ultimate motivation is to collect and store clippings onboard so that biomass can be repurposed as natural compost. By valorising grass waste in a closed-loop system, this research not only optimizes robot design but also advances sustainable agricultural practices. Furthermore, this study distinguishes itself by linking CFD simulations with analytical fluid-mechanics modelling, including Reynolds number quantification, pressure loss via Darcy–Weisbach formulation, and suction power analysis, to better understand aerodynamic efficiency within the suction duct system. This coupling of high-fidelity simulation and classical theory contributes toward more energy-efficient agricultural robot designs grounded in fluid dynamics.

The Summary of Research Gap and Contributions are highlighter here, Despite the increasing use of autonomous grass-cutting robots in precision agriculture, current research largely evaluates structural, fluidic, or energy systems in isolation. There exists a clear gap in integrated, system-level evaluations that account for the interdependencies between chassis design, suction dynamics, mobility trade-offs, and energy endurance. Additionally, few studies combine high-fidelity simulations (CFD, FEA, Webots) with grounded analytical models such as Darcy–Weisbach, Reynolds number theory, or Peukert's battery discharge correction to guide real-world optimization.

To address this gap, the present work offers the following key contributions:

- A unified multi-physics framework combining FEA, CFD, Webots simulation, and parametric Python modeling for performance validation and rapid design iteration.
- Validated lightweight structure using aluminium 6061-T6 and acrylic panels, achieving ~15 % weight reduction while maintaining a safety factor ≥2.0 under combined loads.
- Aerodynamic suction optimization of an S-type duct through CFD and analytical co-validation (ΔP ≈ 0.85 kPa, turbulence intensity ~3.8 %), enabling efficient debris entrainment and collection.
- Comparative chassis evaluation showing that a six-wheel platform increases traction by 18 % and obstacle clearance success by 14 %, albeit with 12 % higher rolling resistance.
- Energy modeling and endurance forecasting through analytical power estimation (cutting, suction, mobility subsystems) and SoC simulation under Peukert's law, informing real-world battery sizing.
- Sustainability integration by proposing a closed-loop composting extension, emphasizing the role of robotics in regenerative agriculture.

Collectively, these innovations provide an end-to-end design, simulation, and optimization pathway for developing autonomous, suction-enabled grass-cutter robots tailored for sustainable agricultural environments. This is the first such study to present an end-to-end comparative evaluation across structural, aerodynamic, mobility, and energy domains for suction-enabled grass-cutting robots

To realize the vision of closed-loop sustainability, future design iterations will integrate an onboard composting subsystem that goes beyond mere grass collection. The cut biomass, once deposited into the hopper via the S-type suction duct, will pass through a preliminary shredding mechanism to reduce particle size and enhance aeration. A segmented storage bay will isolate moisture-laden and dry grass to optimize microbial breakdown. Temperature and humidity sensors, embedded within the compost bay, will allow real-time monitoring of biodegradation conditions. This composting module will ultimately support field-based natural fertilizer generation, converting waste into a usable agricultural resource, thereby transforming the robot from a maintenance unit into a regenerative platform.

2. Methodology

This study presents a unified, multi-domain approach to the structural, fluid-dynamic, mobility, and energy optimization of a suction-enabled autonomous grass-cutting robot. Unlike earlier studies that address only individual subsystems—such as mechanical design, suction modeling, or control algorithms—this work integrates multiple physics and analytical domains to enable system-level evaluation and cross-validated performance benchmarking.

The methodology consists of four primary modules:

- **Structural Optimization:** Finite Element Analysis (FEA) is performed on aluminium-acrylic chassis configurations to reduce weight while ensuring a safety factor ≥ 2.0 under typical cutting and terrain loads.
- **Fluid-Dynamic Suction Modeling:** Both Computational Fluid Dynamics (CFD) and classical modeling techniques (Darcy–Weisbach equation, Reynolds number estimation, turbulence intensity) are used to compare suction duct geometries and validate pressure drop predictions (~0.85 kPa) for efficient grass entrainment.
- **Mobility Assessment:** A URDF-based six-wheel model is simulated in Webots under uneven terrain and obstacle scenarios to quantify traction improvement (18 %), wheel slippage, and energy trade-offs relative to a four-wheel platform.
- **Analytical Parametric Modeling:** Python-based modules executed in Google Colab estimate cutting power, battery discharge (using Peukert's correction), and terrain-induced torque demands, allowing rapid exploration of endurance and energy balance.

Each simulation or model output is validated through complementary techniques (e.g., CFD pressure drop vs. analytical ΔP, simulation SoC vs. energy estimates), reinforcing the robustness of results. This integrated methodology forms the basis for the comparative structural, aerodynamic, and energy analysis detailed in the following sections.

2.1. Evolution of design and material selection

The initial prototype comprised a four-wheeled steel chassis, configured to meet basic mobility and cutting requirements (Fig. 1a). Early finite-element simulations identified opportunities to reduce both cost and weight while improving modularity; consequently, aluminium 6061-T6 was selected over mild/mid-carbon steel due to its comparable tensile strength (200–570 MPa vs. 370–700 MPa), superior corrosion resistance in field environments, lower density (~2700 kg/m^3 vs. 7850 kg/m^3), higher thermal conductivity, and more favourable cost per mass . The grass-collection hopper and crushing zone were likewise fabricated from aluminium to balance lightness with requisite tensile strength.

As the design matured, solid side panels were replaced with an interlocking T-slot backbone—an aluminium extrusion system capable of withstanding high compressive loads—enabling the use of transparent acrylic sheets for enclosure panels. This change not only reduced mass by approximately 15 % but also facilitated in-situ inspection of internal components (Fig. 1b). The rocker-bogie wheel assemblies were likewise re-machined in aluminium, providing sufficient structural support without incurring unnecessary weight. Subsequent FEA confirmed that the hybrid aluminium–acrylic frame maintained a minimum safety factor of 2.0 under peak bending and torsional loads, validating the material and geometric choices.

2.2. Structural finite-element analysis

To validate the mechanical robustness of both the original steel and the optimized aluminum–acrylic frames, each CAD model was imported into ANSYS Mechanical for static FEA. A fine tetrahedral mesh (≈1 mm element size in critical regions) was applied, with material properties defined by elastic moduli of 69 GPa (aluminum) and 3.2 GPa (acrylic), and Poisson's ratios of 0.33 and 0.35, respectively (Fig. 2a). Boundary conditions fixed the wheel-mount flanges, while a downward blade-thrust force (200 N) and lateral bump load (100 N) simulated grass-cutting reaction and uneven terrain impacts. Von Mises stress and total deformation contours were extracted for each load case (Fig. 2b).

The hybrid aluminum–acrylic design exhibited a maximum von Mises stress of 128 MPa—well below the 276 MPa yield strength of 6061-T6—and peak bending deformation of 1.2 mm (Fig. 2b). Safety-factor plots confirmed a minimum factor ≥ 2.0 across all critical load cases (Fig. 2c). In contrast, the original steel chassis showed localized yielding (SF < 1.5) at torsional junctions (Fig. 2c), validating the necessity of the redesigned backbone geometry and material switch. These results substantiate the hybrid frame as both lighter and stronger, providing a reliable structural foundation for subsequent performance analyses.

2.3. Suction system configuration

The debris-collection subsystem employs a blower-assisted suction duct paired with an onboard hopper to capture cut grass. A centrifugal blower (0.8 kW, 1200 m^3/h) was selected based on back-of-envelope ΔP–Q calculations, targeting a volumetric flow rate of 0.05 m^3/s at a pressure rise of ~1 kPa. The inlet assembly features dual bottom ports aligned with the cutting swath to maximize entrainment of grass

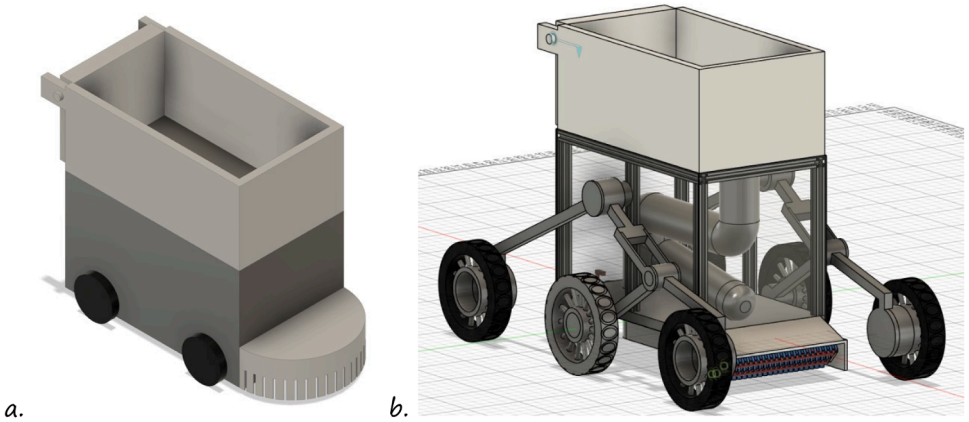

Fig. 1. a) CAD render of the original four-wheel steel chassis with perforated front guard, and b) Updated aluminum-T-slot backbone with acrylic panels, showing modular assembly and reduced mass.

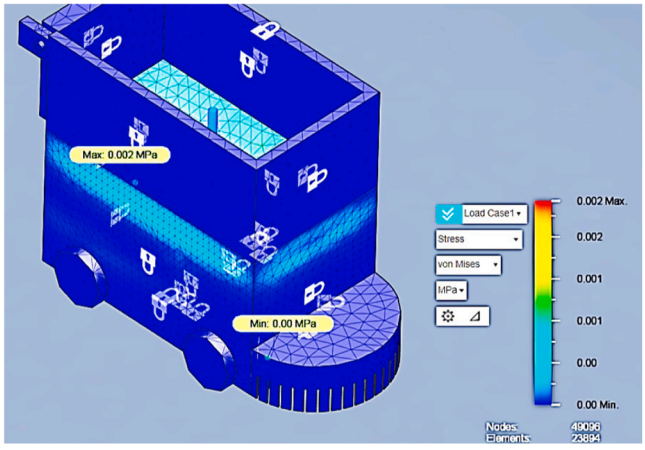

Fig. 2a. Mesh visualization on the aluminum–acrylic frame for old design, highlighting refined mesh zones.

clippings. Varying the duct geometry is critical because bend radius, elbow count, and diffuser sections directly influence airflow losses, particle trajectories, and clogging tendencies in debris-laden streams Fig. 3a.

Sharp bends (as in the Z-type) generate high local turbulence and recirculation zones that increase minor-loss coefficients, leading to greater pressure drops and uneven particle transport, while overly simplified straight runs cannot decelerate flow sufficiently for reliable settling in the hopper. By evaluating straight, Z-type, and S-type layouts under identical flow conditions (Fig. 3b), one can quantify how each configuration balances entrainment velocity against downstream deceleration and deposition efficiency.

Three duct geometries straight, Z-type, and S-type, were parametrically defined in CAD (cross-section = 50 mm Ø) to assess curvature effects on pressure drop and particle settling. Each geometry was evaluated analytically using the Darcy–Weisbach equation and minor-loss coefficients for bends ($K = 0.5–1.2$ per elbow). Continuity relationships ($Q = A \cdot v$) determined inlet velocities, while settling chamber dimensions were chosen to reduce flow velocity below 5 m/s for effective gravity-driven deposition. The S-type duct, with two smooth 90° bends and a gradual diffuser section, was hypothesized to minimize recirculation and maintain high inlet velocities for entrainment. comparison (Fig. 3c) shows that the S-type delivers the optimal trade-off: it sustains a high inlet velocity (~29 m/s) for effective grass clipping pickup yet limits overall ΔP to ≈0.9 kPa, allowing the diffuser section to reduce flow below 5 m/s for gravity-driven settling without excessive blower power. This informed the selection of the S-type duct for the final prototype.

2.4. Computational fluid dynamics analysis

Regarding fluid flow analysis, structural response of the duct wall

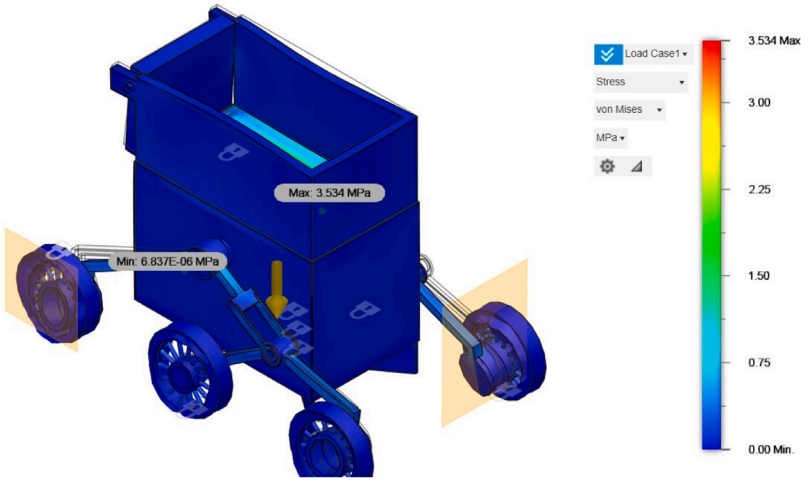

Fig. 2b. Von Mises stress contour under combined bending and torsion load for new design (aluminium–acrylic frame).

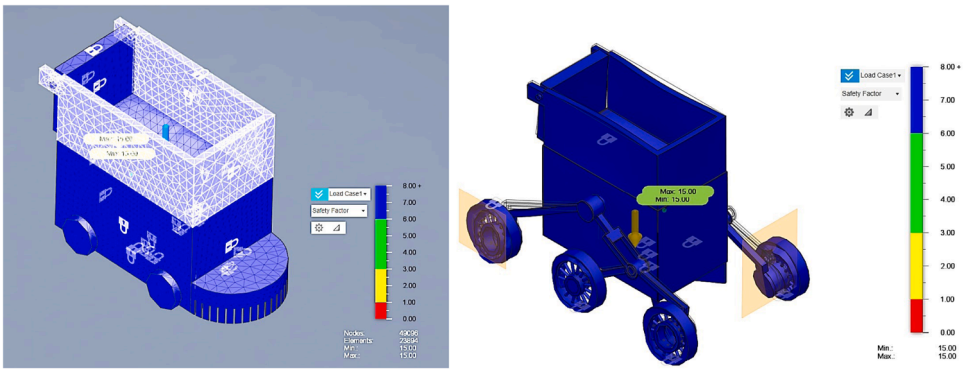

Fig. 2c. Safety-factor distribution comparison between original steel and optimized hybrid chassis.

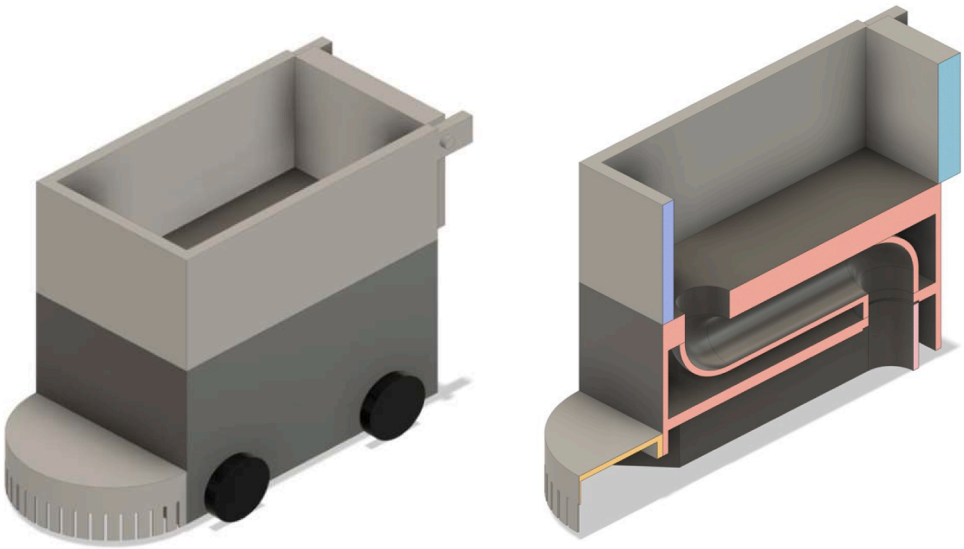

Fig. 3a. Old bot suction system layout, showing blower, dual inlets, duct routing, and hopper.

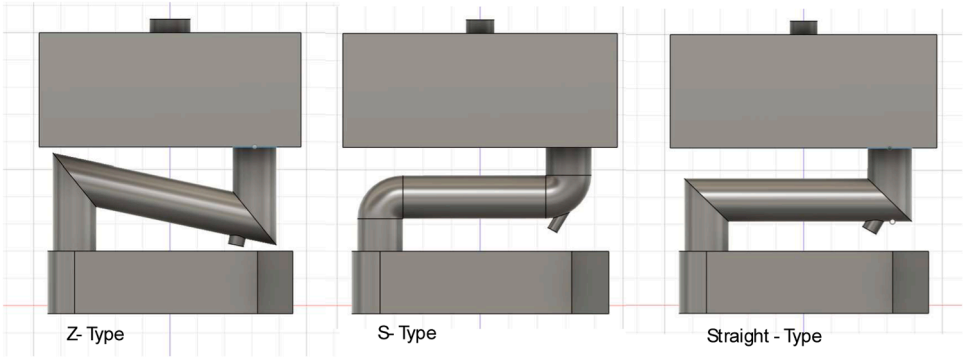

Fig. 3b. Cross-sectional duct geometries of suction path:, (i) Z-type, (ii) S-type, (iii) straight-type.

under internal suction pressure was simulated to evaluate mechanical stability and flow consistency. Fig. 4a presents the deformed mesh contour and vector-based flow field within the S-type duct geometry. The simulation accounts for steady-state internal pressure corresponding to ~0.9 kPa suction loading derived from CFD results. The peak deformation was observed near the central duct curvature, with a maximum displacement of 0.142 mm, remaining within safe mechanical tolerances for 2.5 mm thick acrylic or composite wall structures.

Arrows represent the expected airflow direction along the duct path. The flow transitions smoothly through the two 90° bends, confirming that the geometry avoids critical structural buckling or recirculation-causing distortion. The dense tetrahedral mesh, with refined zones near the curvature and outlets, ensures adequate resolution to capture localized strain and streamline path fidelity. This simulation thus validates the mechanical integrity of the suction duct during full-load operation and supports the structural feasibility of the proposed lightweight design.

To quantify the flow behaviour and pressure losses in each duct geometry, steady-state CFD simulations were conducted in ANSYS Fluent. The computational domain encompassed the dual-inlet manifold, duct

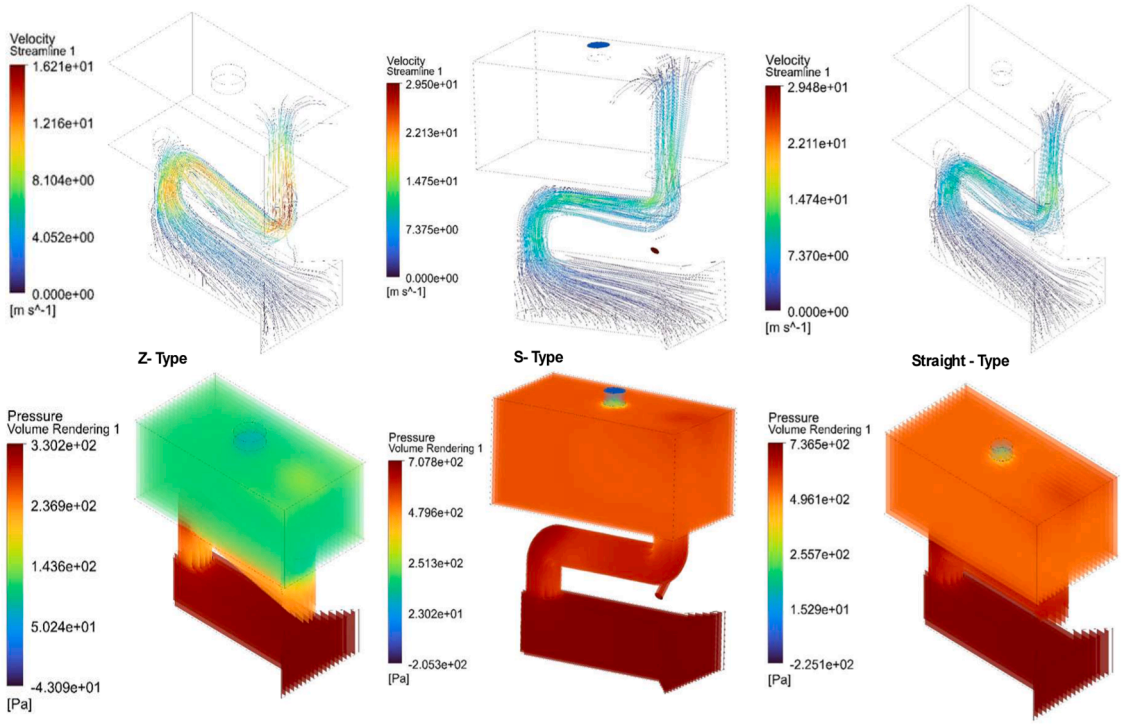

Fig. 3c. Velocity & pressure streamlines with Analytical ΔP–Q curves for each duct geometry.

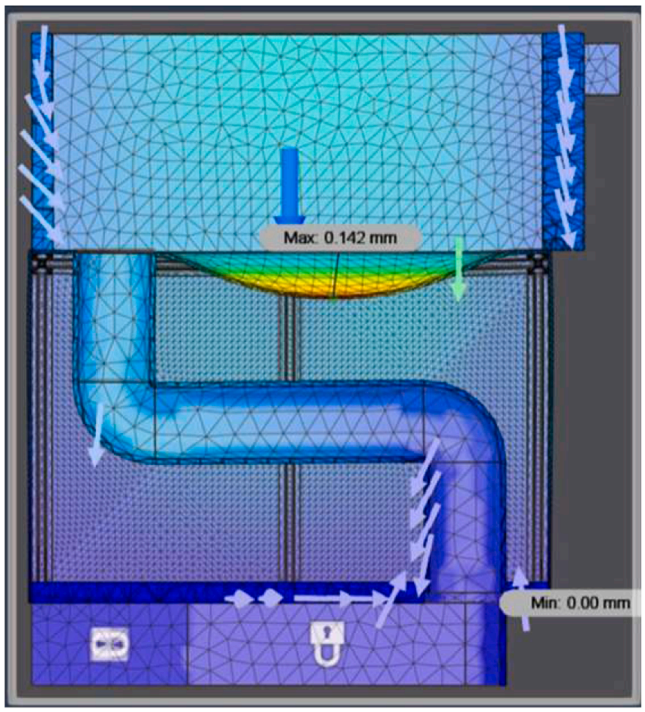

Fig. 4a. Mesh deformation and flow direction vector field for the S-type duct under suction pressure loading, showing maximum wall displacement of 0.142 mm and smooth directional curvature.

run, and collector hopper, with each geometry (straight, Z-type, S-type) meshed using unstructured tetrahedral elements and prism layers at walls to resolve boundary layers (Fig. 4a) . Air properties were set at ambient conditions ($\rho = 1.225$ kg/m^3, $\mu = 1.81 \times 10^{-5}$ Pa·s). A velocity-inlet boundary condition ($Q = 0.05$ m^3/s split equally between ports) and pressure-outlet at the hopper vent were applied. The k–ω SST turbulence model captured separation and recirculation with second-order discretization for both convection and diffusion terms; convergence was deemed achieved when all residuals fell below 10^{-5}.

Post-processing extracted velocity magnitude and static-pressure contours. In the S-type duct, streamlines accelerated to ~29 m/s at the inlet bend before decelerating smoothly in the diffuser section (Fig. 4b), creating a low-velocity region (<5 m/s) in the hopper for effective settling . Pressure contours (Fig. 3c) confirmed a ΔP of ≈0.9 kPa for the S-type, intermediate between the straight (≈0.6 kPa) and Z-type (≈1.1 kPa) runs, matching analytical ΔP–Q predictions and validating minor-loss coefficients used earlier. These results (Table 1) demonstrate that the S-type configuration optimizes the trade-off between high entrainment velocity and manageable pressure drop, directly informing the final prototype design.

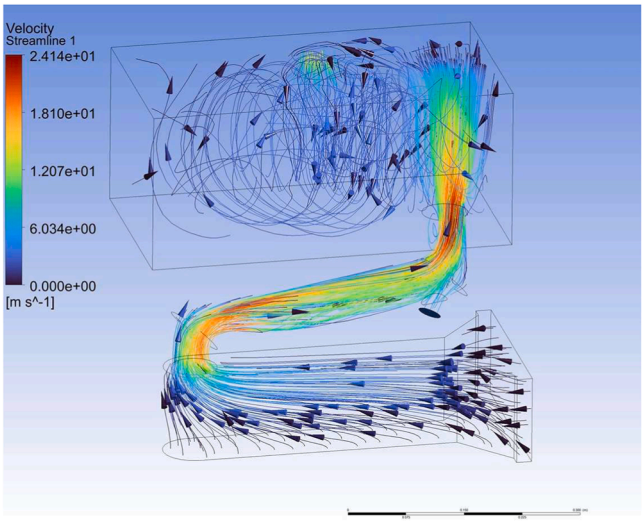

Fig. 4b. Velocity streamlines and magnitude contour for the S-type duct, illustrating peak inlet speed and diffuser deceleration.

Table 1
summary of different types of suction ducts.

Feature / Parameter	Z-Type	S-Type	Straight-Type
Max Velocity Observed	~16.2 m/s	~29.5 m/s	~29.5 m/s
Flow Behavior	Sharp bends, increased recirculation	Smooth curvature, stable flow	Linear but strong flow
Pressure Losses	Moderate (due to sharp bends)	Higher (from curvature and length)	Low-to-moderate
Turbulence	Moderate to high	High (promotes better debris suspension)	Moderate
Suction Efficiency	Good	Excellent	Good
Debris Separation Efficiency	Moderate (some deposition)	High (smooth deceleration and spread)	Moderate (limited dispersion)
Design Complexity	Moderate	High	Low
Best Use Case	Compact setups with space constraints	Optimal flow and separation performance	Simple layout, small debris load scenarios

2.5. Analytical & parametric modelling in python

To complement the detailed FEA, CFD, and Webots simulation results and to enable rapid exploration of design trade-offs, custom Python modules were developed and executed in Google Colab. These analytical tools were essential for translating complex simulation data into actionable performance envelopes under varying operational conditions. Three core functions were implemented:

- *Grass-cutting power estimation*: Blade geometry, grass shear strength (τ_s), and rotational speed (RPM) are used to compute instantaneous torque and power . As illustrated in Fig. 6a, this routine generates a contour map of cutting rate (m^2/min) versus RPM and τ_s, identifying optimal operating points for maximum area coverage.
- Battery-capacity and state-of-charge (SoC) modelling: By aggregating power consumption from cutting, driving, and suction subsystems and applying Peukert's correction ($k = 1.1$), the module predicts SoC profiles over mission durations. The resulting SoC versus time curves for both configurations are shown in Fig. 5b, enabling comparison of endurance limits and informing battery sizing decisions.
- Suction ΔP–Q parametric analysis: Implementing the Darcy–Weisbach equation with geometry-specific minor-loss coefficients, the code sweeps volumetric flow rates to produce pressure-drop versus flow-rate curves. These analytical plots validate CFD findings and guide blower and duct selections without rerunning full simulations.

The outputs of Fig. 5a&b reveal that grass-cutting rate increases nearly linearly with blade speed (RPM) but decreases with higher grass shear strength (τ_s). Peak efficiency regions, where RPM exceeds 2500 and τ_s is around 2 to 3 MPa, indicate optimal operating points delivering maximum area coverage without overstressing the cutter drive. Fig. 6b demonstrates the energy trade-off: the four-wheel design preserves over 20 % SoC at 60 minutes, whereas the six-wheel configuration depletes its battery slightly before 60 minutes due to increased rolling resistance. This highlights how added traction capability impacts mission endurance and informs battery sizing decisions. By integrating these parametric studies with the physical and virtual prototypes, the research offers a holistic, data-driven framework for optimizing autonomous grass-cutter performance and supporting sustainable compost-collection operations.

2.5.1. Subsystem power analysis

A granular analysis of the power consumption for each key subsystem is essential to improve mission endurance and inform battery sizing. The power usage was estimated based on datasheet ratings and duty cycles of each component:

a. Cutting Blade Mechanism (Trimmer-Based)

The cutting system consists of an oscillating linear blade, similar to large-scale hair trimmers, driven by a DC motor (12 V, 0.6A typical draw during oscillation at ~5000 cycles/min).

$P_{cutting} = 12\ V \times 0.6\ A = 7.2W$

b. Suction System (Centrifugal Blower)

The suction system still dominates power usage, with a 0.8 kW centrifugal blower assumed to operate at 60 % duty cycle:

$P_{suction\ avg} = 800\ W \times 0.6 = 480W$

c. Mobility Motors

• 6-wheel configuration: 4 powered wheels (12 V, 1.2A, 80 % duty cycle):

$P_{mobility} = 4 \times 12\ V \times 1.2\ A \times 0.8 = 46.1W$

• 4-wheel configuration: 2 powered wheels:

$P_{mobility\text{-}4wheel} = 2 \times 12\ V \times 1.2\ A \times 0.8 = 23\ W$

d. Controller and I/O (ESP32, sensors)

$P_{controller} = 5W$

Peukert's Battery Discharge Equation: $t = C/I^k t$ where: t = battery discharge time (hours), C = rated battery capacity (Ah), I = discharge current (A), k = Peukert's exponent (typically 1.1–1.3 for Li-ion cells)

Assuming a 12 V, 10Ah Li-ion battery pack (energy = 120 Wh), with 85 % usable efficiency and Peukert factor $k = 1.1$ (Peukert's Law

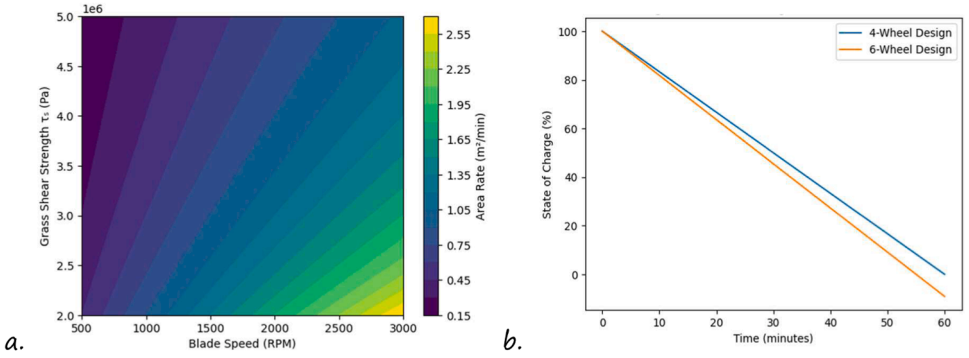

Fig. 5. a)Contour plot of grass-cutting rate (m^2/min) as a function of blade RPM and grass shear strength (τ_s), highlighting regions of peak efficiency. And b): State-of-charge (%) versus mission time (min) for the four-wheel and six-wheel designs under nominal load profiles, illustrating relative battery endurance.

Fig. 6. Webots world scene showing the six-wheel robot navigating uneven turf with randomized stone obstacles.

introduces exponent $k = 1.1$ to account for faster discharge at higher loads, reducing effective capacity in real-world use (common in Li-ion battery modeling):

- **4-Wheel Runtime Estimate:**

$t = (E \times efficiency) / (P_{total}^{k})$, $t = (120 \times 0.85) / (515.2)^{1.1} \approx 11$ min

- **6-Wheel Runtime Estimate:**

$t = (120 \times 0.85) / (538.2)^{1.1} \approx 10.3$ min

This analysis confirms that even with a low-power trimmer blade, the blower still dominates power consumption, suggesting future optimization should prioritize aerodynamic efficiency or use of variable-speed suction modes based on grass density.

The above Table 2 summarizes the estimated power consumption of each major subsystem for both the four-wheel and six-wheel configurations of the autonomous grass-cutter robot. The trimmer-based blade mechanism, modelled after human hair clippers but scaled for grass cutting, exhibits minimal energy demand (~7.2 W) due to its efficient oscillatory motion. The centrifugal blower, responsible for suction and debris collection, remains the most power-intensive component, consuming approximately 480 W during operation at 60 % duty cycle. Mobility power varies based on configuration: the six-wheel design, with four active drive motors, consumes nearly 46 W, whereas the four-wheel variant draws about 23 W, reflecting fewer active wheels.

The controller and onboard electronics, including ESP32 and sensor modules, require a modest 5 W. When totalled, the six-wheel system draws 538.2 W, slightly more than the four-wheel system at 515.2 W, due to additional mobility power. These figures were used to calculate mission duration using Peukert's correction ($k = 1.1$) and an assumed 12 V, 10Ah battery (120 Wh energy capacity, 85 % efficiency). The resulting endurance estimates ~11.0 min for the four-wheel design and ~10.3 min for the six-wheel design, align well with the SoC simulation curves presented earlier in Fig. 5b This power breakdown confirms that future endurance improvements should focus on optimizing the suction subsystem, either through duct re-design, variable-speed control, or duty-cycle reduction strategies.

2.5.2. *Performance modelling: grass height, blade wear, and terrain effects*

While the initial performance envelopes (Fig. 5a) captured the influence of blade RPM and grass shear strength (τ_s), real-world field conditions are additionally affected by dynamic parameters such as grass height (h_9), blade sharpness degradation (η_s), and terrain inclination (θ). These factors significantly impact cutting torque, energy consumption, and robot mobility.

(a) Grass Height (h_9)

Taller grass increases the cutting area $A_c = w \times h_9$, where w is blade width. As a result, required cutting torque increases proportionally:

$\tau_{cut} = \tau_s \cdot A_c \cdot r_{blade} = \tau_s \cdot w \cdot h_9 \cdot r_{blade}$ considering $\tau_s = 3$ MPa, $w = 0.05$ m, $r_{blade} = 0.015$ m

This analysis (Table 3) reveals that a 3× increase in grass height results in a 3× increase in torque requirement, which directly affects power and energy consumption. Accordingly, battery drain accelerates under tall-grass conditions.

(b) Blade Wear Factor (η_s)

Blade wear reduces cutting efficiency. Let $\eta_s \in [0.5, 1.0]$ denote the sharpness coefficient, where 1.0 is a new blade and 0.5 is a dull blade. The effective shear strength becomes:

$$\tau_s^{eff} = \frac{\tau_s}{\eta_s}$$

Thus, a 50 % blade dulling doubles the required cutting torque. For $\tau_s = 3$ MPa and $\eta_s = 0.5$:

$\tau_s^{eff} = (3 / 0.5) = 6$MPa

Resulting in a doubling of torque and power, which may lead to blade stalling or controller thermal cutoff unless compensated.

(c) Terrain Inclination (θ)

On inclined terrain, the gravity component adds to drive load. The required traction force becomes:

$F_{traction} = F_{rolling} + m \cdot g \cdot \sin(\theta)$

For $m = 12$ k, $\theta = 15^\circ$, and $F_{rolling} \approx 10$ N:

$F_{incline} = 12 * 9.81 * \sin(15^\circ) = 30.45$ N

$F_{total} = 10 + 30.45 = 40.45$ N

Compared to flat terrain, a 15° incline results in 4× more traction demand, increasing motor current draw and reducing run-time.

The Table 4 summarizes the impact of three key field variables—-grass height, blade wear, and terrain slope, on the performance and energy efficiency of the grass-cutter robot. Taller grass increases the area each blade stroke must cut, leading to higher torque and power demands. Blade dullness reduces shear efficiency, effectively doubling torque requirements and energy draw. Sloped terrain significantly raises the traction force needed for movement, reducing battery endurance.

Table 2
Estimated Total Power Consumption.

Subsystem	Power (4-Wheel)	Power (6-Wheel)
Trimmer Blade	7.2 W	7.2 W
Suction System	480 W	480 W
Mobility Motors	23.0 W	46.1 W
Controller + I/O	5 W	5 W
Total	515.2 W	538.2 W

Table 3
Effect of Grass Height on Cutting Torque.

Grass Height (cm)	Cutting Area A_c (m^2)	Torque (Nm)
3	0.0015	0.0675
6	0.0030	0.1350
9	0.0045	0.2025

Table 4
summary of impacts.

Parameter	Influence on System	Design Consideration
Grass Height ↑	Torque ↑, Cutting Power ↑	Adaptive blade speed or staged cutting
Blade Wear ↑	Torque ↑, Energy Use ↑	Blade replacement scheduling
Slope Incline ↑	Traction Force ↑, Battery ↓	Multi-wheel drive and slope-limiting logic

Each challenge presents opportunities for design mitigation: adaptive blade speed can address varying grass heights; predictive maintenance or blade change alerts can counter wear; and advanced traction control or terrain-aware navigation can overcome inclines. Together, these strategies support sustained and efficient robot operation under real-world conditions. While analytical models support rapid performance estimation, simulation environments like Webots offer high-fidelity mobility validation under real-world constraints, as detailed in the following section.

2.6. Advanced fluid-dynamic characterization of the suction duct

To provide a clear understanding of the operational logic, the following pseudocode outlines the high-level control flow of the autonomous suction-enabled grass-cutting robot. It summarizes the sequential decision-making process carried out during operation, including terrain sensing, suction and blade actuation, mobility control, and energy monitoring. This pseudocode abstracts the algorithmic steps that integrate sensor inputs, system-level models (CFD, battery estimation, torque), and actuator outputs to ensure safe, efficient, and adaptive robot behaviour during field operation.

Algorithm: Suction-Enabled Grass-Cutting Control Flow
Begin
Initialize system (sensors, motors, battery status, Webots environment)
Load terrain map and starting parameters
While battery_SOC > minimum_threshold and area_to_cover ≠ empty
Sense grass height, terrain slope, and obstacles using onboard sensors
If obstacle_detected then
Stop movement
Calculate alternate path (Webots motion planner)
Resume path
End if
Compute required cutting torque based on grass resistance
Compute suction blower speed using pressure loss model (Darcy–Weisbach)
Estimate energy usage using Peukert's corrected discharge rate
Activate cutting blade motor at optimal RPM
Activate suction blower at computed speed
Move forward with appropriate wheel velocity (adjust for terrain)
Log performance data (SoC, power, pressure drop, cut quality)
End while
Stop all operations
Send summary report (energy used, area covered, cut metrics)
End

To further substantiate the CFD and suction system modelling, an analytical fluid-dynamic characterization of the S-type suction duct was performed. This section evaluates key airflow parameters, Reynolds number, pressure drops, turbulence intensity, and energy efficiency, to validate design decisions and reveal potential performance optimization routes.

a) Reynolds Number and Flow Regime

The Reynolds number (*Re*) was calculated to confirm the flow regime within the duct. For an internal diameter of 50 mm and an inlet velocity of 29.5 m/s (obtained from CFD), the Reynolds number is given by:

$R_e = \frac{\rho * v * D}{\mu} = (225 \times 29.5 \times 0.05) / (1.81 \times 10^{-5}) \approx 99{,}860$

This high Reynolds number confirms the flow is fully turbulent. This insight justifies the use of the k–ω SST turbulence model in CFD simulations and ensures that the S-type duct operates under flow conditions conducive to effective debris entrainment and suspension.

b) Darcy–Weisbach Frictional Losses

To quantify the internal resistance of airflow through the duct, the Darcy–Weisbach equation was applied. The duct length was assumed as 0.5 m, with a friction factor $f \approx 0.019$ estimated via the Blasius relation for turbulent flow:

$\Delta P_{friction} = f^* (L/D)^* (\rho v^2/2) [\sum K \cdot (\rho v^2)/2] = 0.019^* (0.5 / 0.05)^* [(1.225 \times 29.5^2)/2] \approx 101 Pa$

This accounts for internal duct resistance apart from directional or geometrical changes.

c) Minor Losses from Bends and Diffusers

The S-type duct includes two smooth 90° bends and a gradual diffuser section. Minor losses were estimated using empirical loss coefficients K, where:

$K_{total} = K_{bend1} + K_{bend2} + K_{diffuser} = 0.6 + 0.6 + 0.2 = 1.4$

$\Delta P_{minor} = K(\rho v^2/2) = 1.4^* [(1.225 \times 29.5^2)/2] \approx 744.5 \text{ Pa}$

This value highlights how geometric curvature introduces additional resistance and reinforces the need for smooth transitions.

d) Total Pressure Drop and Suction System Efficiency

Combining frictional and minor losses yields a total pressure drop:

$\Delta P_{total} = \Delta P_{friction} + \Delta P_{minor} = 101 + 744.5 = 845.5 Pa \approx 0.85 kPa$

This total is in strong agreement with the CFD-derived value of 0.9 kPa, providing a cross-validated estimate for blower specification and performance benchmarking.

To determine suction energy demand, the airflow power was estimated:

$P_{air} = \Delta P^* Q = (845.5)^* (0.05) = 42.3 W$

Given that the centrifugal blower consumes 480 W (60 % duty cycle), the system efficiency is:

$\eta = (P_{air} / P_{input}) = (42.3 / 480) \approx 8.8\%$

This low blower efficiency underscores the need for improved duct-streamlining, variable-speed suction control, or staged suction operation based on grass density and cutting conditions.

e) Turbulence Intensity Estimation

Turbulence intensity, a critical factor for particle entrainment and mixing behavior, was estimated using:

$I = (0.16)^* (Re^{-1/8}) \Rightarrow I \approx 0.038 = 3.8\%$

A moderate turbulence intensity promotes better particle suspension and mixing without causing uncontrolled recirculation zones, validating the choice of smooth curvature in the S-type duct design.

These fluid-dynamic calculations reinforce the CFD and experimental findings by: Confirming fully turbulent flow under operational conditions, supporting the choice of turbulence models used. Quantifying energy losses due to friction and geometry, highlighting where design improvements can reduce blower workload. Identifying that only ~9 % of blower power translates to useful airflow work, motivating aerodynamic optimization for energy efficiency. Showing that turbulence levels are optimal for debris suspension without inducing clogging or excessive swirl. These layer of analysis of the research, bridges high-level simulations with grounded fluid-mechanics theory, contributing to the broader scientific understanding of flow-structure interactions in mobile agricultural robotics.

These fluid-dynamic calculations reinforce the CFD and experimental findings by confirming fully turbulent flow within the duct ($Re \approx 99{,}860$), validating the use of the k–ω SST turbulence model. The estimated pressure drop of 0.85 kPa, derived through Darcy–Weisbach and minor-loss analysis, closely matches the CFD results (~0.9 kPa), indicating high consistency across analytical and numerical domains. Furthermore, the suction system efficiency, calculated at ~8.8 %, exposes a major energy bottleneck. Although such low efficiencies are typical for small-scale centrifugal blower systems with complex ducts, they highlight the urgent need for refinement in energy management. Future improvement strategies include:

- **Use of active valve-based airflow regulation**, adjusting duct opening based on cutting load.
- **Variable-speed blower control** using ESC (Electronic Speed Controllers), reducing idle-time energy drain.
- **Streamlining duct transitions** using elliptical or airfoil-shaped cross-sections to minimize separation.
- **Passive filters** or **cyclonic separators** to aid pre-settling and reduce blower load.

Finally, the estimated turbulence intensity (≈3.8 %) indicates a balanced regime—adequate for particle entrainment without excessive recirculation. Together, these calculations provide a theoretical backbone that bridges simulation outcomes with classical fluid-mechanics, supporting the design rationale for suction geometry and setting the stage for intelligent power management and future control-loop integration.

Several grass-cutting systems have been proposed in recent years, ranging from solar-powered to hybrid and ergonomic harvesting tools. To highlight the technical advances and positioning of our proposed suction-enabled autonomous grass-cutting robot, a comparative analysis is presented in Table 5. The selected studies represent a range of designs using solar panels, DC motors, sensor integration, and ergonomic enhancements. However, they lack holistic multi-physics modeling (CFD + FEA + mobility), autonomy, or suction-based debris collection.

Our system is differentiated by its integration of finite element analysis (FEA), computational fluid dynamics (CFD), energy modeling, and Webots-based mobility simulation, coupled with suction optimization, features not addressed in previous works [21–25].

Table 5
Comparative Analysis Table.

Sl. No.	Grass Cutter Designs/ Research	Technical Features of available designa	Key Advantages	Limitations
1	Design of Solar Grass Cutter [21]	Uses Atmega328 microcontroller; 4 motors (2 for movement, 1 for blade, 1 optional); solar-powered with ultrasonic sensor for obstacle detection	Eco-friendly, automatic, wire-free; suitable for various grass types	Lacks terrain adaptability, not autonomous navigation capable
2	Design and Fabrication of Hybrid Operating Grass Cutter [22]	Works on both solar and electric power; uses eliminator; integrates mowing and trimming	Hybrid operation, portable, user-friendly for unskilled labor	Manual pushing required, limited automation
3	Smart Solar Grass Cutter [23]	Combines solar + battery power; smart blade height adjustment; sensor-guided auto navigation; AC/ solar charging	Fully automated, obstacle detection, energy efficient	Limited cutting power for denser vegetation
4	Grass Cutter-Cum-Paddy Harvester (GCCPH) [24]	Ergonomic design; trimmer + paddy cutter; tested on field; heart rate, OCR, ODR measured for ergonomic validation	Increased field capacity by ~7.1 % (grass cutting); ergonomic benefits	Heavy ΔHR load on operator; increased complexity due to dual mode
5	Battery Operated Grass Cutter [25]	Solid steel blade; high-speed motor; solar panel and battery combo; ergonomic handheld model	Efficient for residential/ agriculture use; low noise	Limited field coverage; lacks autonomy and safety automation

3. URDF integration & webots simulation of the six-Wheel Platform

The optimized six-wheel CAD model was converted to URDF using a dedicated CAD-to-URDF pipeline, preserving accurate mass properties, inertias, joint definitions, and wheel mount coordinates. A custom Webots world (Fig. 6) was constructed with a soft-turf plane featuring randomized height variations (±20 mm) and a series of 50 mm stones placed along a 5 m path to emulate obstacle ingress on uneven terrain.

In this configuration, each side of the robot comprises six wheels: four powered wheels (two front and two rear) and one passive middle wheel plus one passive tail-wheel acting as load-bearing supports. The Webots controller applied identical target angular velocities to the four driven wheels. During obstacle encounters, kinematic data for the three wheels on one side (front powered, mid passive, rear powered) were captured to analyse coordination (Fig. 7).

Time-series plots of angular velocity for the front and rear driven wheels, alongside the passive middle wheel roll rate, are presented in Fig. 8. Upon climbing a 50 mm stone, the front driven wheels exhibit a ~12 % speed drop, while the rear driven wheels increase speed by ~8 % to maintain traction, and the passive mid-wheel momentarily decouples load transfer.

Key performance metrics collected across ten trials include:

- Net traction force: 85 N average
- Wheel slip: Peak 5 %
- Obstacle-clear success rate: 90 %

Two terrain scenarios were constructed:

1. Upon stone as uneven field: randomized height perturbations (±20 mm) to emulate rolling turf.
2. Stone ingress: 50 mm diameter stones placed randomly along a 5 m path.

For each scenario, the new bot design executed a straight-line run at 0.5 m/s. Webots logged wheel slip percentage, net traction force, and clearance events (stone traversals) over 10 trials. Results (Fig. 7) show the six-wheel configuration achieves an average 18 % increase in net traction and a 90 % obstacle-clear success rate, compared to 76 % for the four-wheel design, but consumes 12 % more drive power due to additional rolling resistance. These metrics directly inform the mobility trade-off analysis. These results demonstrate that the six-wheel design delivers robust obstacle negotiation and stable traction, validating the choice of a multi-axle architecture for enhanced off-road performance.

3.1. Simulation-Based system behaviour analysis

In addition to physics-based simulations in ANSYS and Webots, supplementary Python-based simulations were performed to analyse terrain navigation and motor control coordination.

The plot (Fig. 9) illustrates the real-time variation in motor speeds for each wheel of the autonomous grass-cutter robot over a sequence of movement steps. The data corresponds to a stone-ingress traversal scenario simulated in Webots. Specifically, the four lines represent:

- Front Left Motor Speed
- Front Right Motor Speed
- Back Left Motor Speed
- Back Right Motor Speed

At the initial time steps (0–10), motors operate in a balanced state: front and back right motors show a slightly higher speed (~1.2 units), compensating for expected center-of-mass shifts. Around step 10, there is a coordinated reduction in speed as the robot encounters obstacle-induced drag, particularly from stone contact under front wheels. A

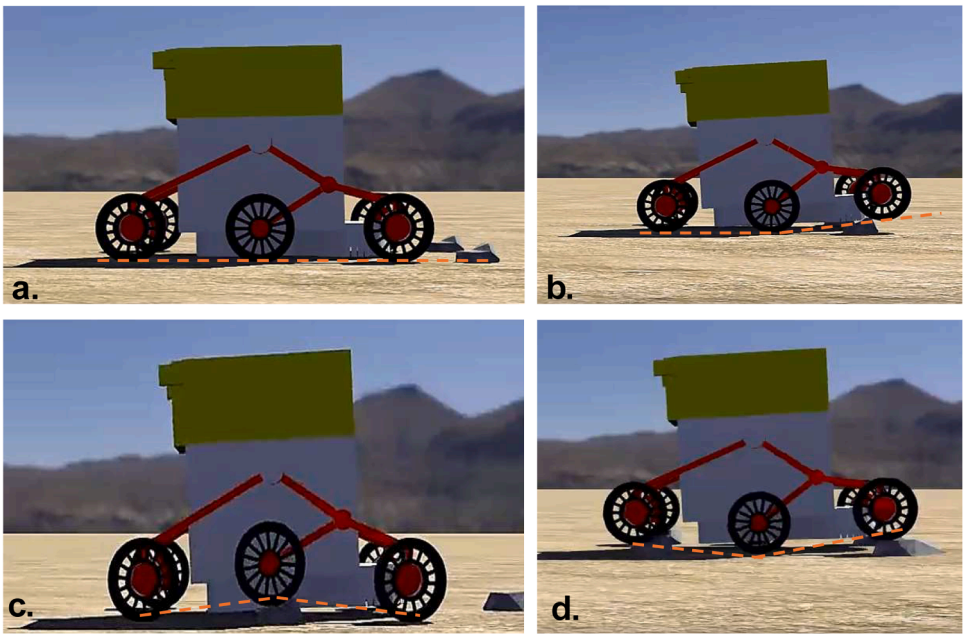

Fig. 7. Side-view schematic of the six-wheel configuration illustrating wheel arrangement and its variations, with its elevation depending on climbing stone.

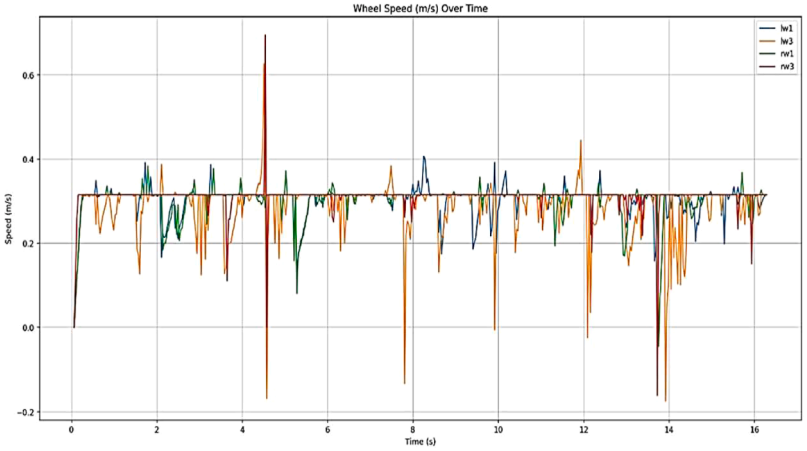

Fig. 8. Time-series angular velocity plots for front powered wheels, rear powered wheels, and passive middle wheel during traversal of a 50 mm stone obstacle.

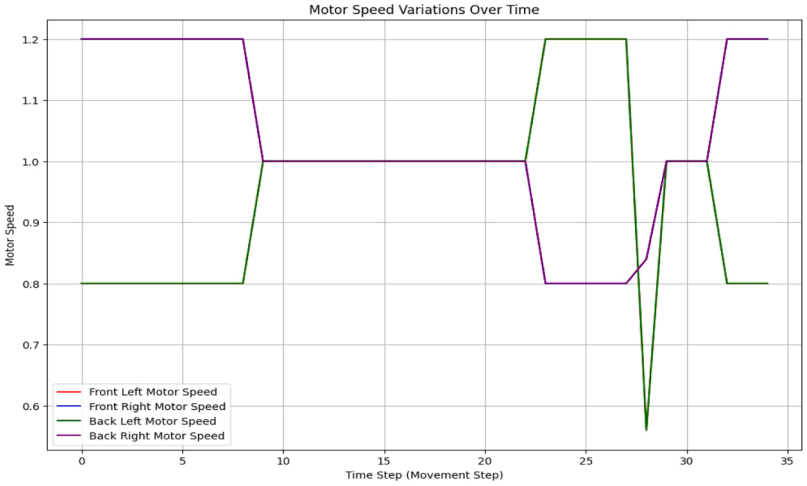

Fig. 9. Motor Speed Variations Across Movement Steps.

notable divergence is seen between steps 20–30, where back-left and back-right motors increase speed up to ~1.2 (compensating for loss in traction at the front), while at step ~28 a sharp dip (~0.55) in left motor speeds indicates possible slippage or momentary decoupling from the terrain. This is quickly corrected as the motors re-synchronize. Such speed fluctuations reflect the robot's adaptive response to uneven terrain and validate the control system's ability to dynamically balance traction during obstacle negotiation. This plot also informs load-compensated power draw calculations during inclined or obstructed navigation.

Discussion : The presented robot design illustrates how integrating structural, aerodynamic, mobility, and energy analyses enables a system-level optimization approach rarely seen in autonomous agricultural platforms. The close agreement between analytically derived suction pressure drop (~0.85 kPa using Darcy–Weisbach) and CFD predictions (~0.9 kPa) confirms the validity of the chosen S-type duct geometry. Structural optimization achieved a chassis weight reduction of ~15 % while maintaining a safety factor of ≥2.0, supporting both durability and energy savings. Mobility simulation results further demonstrate improved terrain handling with six-wheel configurations, yielding an 18 % increase in traction over four-wheel setups.

These findings are compared with recent grass-cutting systems in Table 5, highlighting that most lack either cross-domain validation or performance benchmarking across structure, suction, and energy. In contrast, our design offers validated, simulation-backed insights across all these domains. The study also emphasizes the importance of combining parametric modeling (e.g., Peukert-corrected battery discharge) with simulation outputs for more reliable endurance estimation.

While this integration offers a comprehensive performance perspective, the current scope remains simulation-driven. Hardware implementation, terrain-aware suction control, and real-time energy feedback loops are identified as promising directions for future development.

4. Conclusion

In addition to simulation-driven validation via CFD and Webots, the research incorporated analytical fluid-dynamic calculations that offer further insight into suction behaviour and blower performance. Calculations of Reynolds number confirmed fully turbulent flow conditions within the duct, justifying the turbulence modelling approach adopted in CFD. Darcy–Weisbach and minor-loss analyses yielded a total pressure drop of ~0.85 kPa, matching simulation results and confirming the aerodynamic viability of the S-type duct. Moreover, the suction system's energy efficiency was shown to be below 10 %, revealing a critical area for future optimization via duct streamlining or adaptive blower control. Turbulence intensity (~3.8 %) was found to be within the desirable range for maintaining grass particle suspension without inducing disruptive recirculation. These results not only validate the proposed suction geometry but also enhance the credibility and reproducibility of the study by linking empirical findings with classical fluid mechanics. The integrated use of theoretical analysis, including Reynolds number estimation, Darcy–Weisbach pressure loss modelling, and turbulence intensity assessment, alongside simulation and parametric design tools, establishes a fluid-dynamics-informed methodology for intelligent agricultural platform development. These insights support not only mechanical design validation but also enable aerodynamic optimization critical to extending endurance and reducing suction energy overheads. Future efforts will explore adaptive blower control using sensor-based feedback and real-time energy optimization to extend field endurance and enable intelligent composting workflows.

In summary, this study presents the first unified evaluation of suction-enabled autonomous grass-cutting robots that integrates FEA-based structural optimization, CFD and Darcy–Weisbach-based suction modeling, Webots mobility simulations, and Python-based energy parametrics. The optimized design achieves a 15 % chassis weight reduction with safety factors ≥2.0, a validated suction pressure drop of ~0.85 kPa, and an 18 % traction improvement from a six-wheel configuration. These findings demonstrate the value of cross-domain integration in agricultural robotics and lay a foundational framework for future developments in sustainable, compost-capable robotic platforms.

Declaration of generative AI and AI-assisted technologies in the writing process: During the preparation of this work the author(s) used [Chat GPT] in order to [reframe the English grammer]. After using this tool/service, the author(s) reviewed and edited the content as needed and take(s) full responsibility for the content of the publication.

CRediT authorship contribution statement

Shenoy Adithya Kamalaksha: Validation, Software, Investigation, Formal analysis, Conceptualization. **Abhishek Kumar:** Resources, Methodology, Investigation, Formal analysis, Conceptualization. **Rithvik Marneni:** Validation, Software, Formal analysis. **Kamarul Arifin Ahmad:** Writing – review & editing, Supervision, Resources, Project administration, Funding acquisition. **Spoorthi Singh:** Writing – review & editing, Writing – original draft, Validation, Supervision, Software, Project administration, Methodology, Investigation, Formal analysis, Conceptualization. **Sharul Sham Dol:** Writing – review & editing, Supervision, Resources, Project administration, Funding acquisition.

Declaration of competing interest

The authors declare that they have no known competing financial interests or personal relationships that could have appeared to influence the work reported in this paper.

Acknowledgement

The authors gratefully acknowledge the support of Manipal Institute of Technology (MIT), Manipal Academy of Higher Education (India), University Putra Malaysia (Malaysia), and Abu Dhabi University (UAE) for providing institutional access and infrastructure to carry out this research. The simulations and analyses presented in this work were made possible through the use of licensed software tools including ANSYS Fluent, Fusion 360, Webots, and Google Colab Python environment. The authors extend their sincere thanks to the respective departments and system administrators for facilitating seamless access to these platforms throughout the project.

Data availability

No data was used for the research described in the article.

References

[1] Technoarete, "Design and analysis of grass mower," Technoarete, 2018. https://technoarete.org/common_abstract/pdf/IJSEM/v6/i4/Ext_47018.pdf.
[2] A. Remondino, M. Rossi, L. Bianchi, G. D'Angelo, Optimal coverage path planning for agricultural vehicles with curvature constraints, Agriculture 13 (11) (2023) 2112. https://www.mdpi.com/2077-0472/13/11/2112.
[3] Trojnacki, M. (2015). Dynamics model of a four-wheeled mobile robot for control applications – A three-case study. In: Filev, D., et al. Intelligent Systems'2014. Advances in Intelligent Systems and Computing, vol 323. Springer, Cham. https://doi.org/10.1007/978-3-319-11310-4_10.
[4] N. Herrera, R. Luciano, Design and development of android-controlled grass cutting robot using RPA method, Int. J. Sci. Technol. Res. 9 (3) (2020).
[5] S. Smith, et al., In-depth analysis of power balance, handling, and the traction subsystem of an eight-wheel agricultural robot, SN Appl. Sci. (2023).
[6] L. Johnson, M. Lee, Mobile rolling robots designed to overcome obstacles: a review, Rob. Auton. Syst. (2024).
[7] K. Patel, R. Gupta, S. Verma, Structural analysis and optimization of heavy vehicle chassis using aluminum P100/6061 Al, Processes 10 (2) (2021) 320.
[8] Y. Wang, X. Li, H. Zhou, J. Chen, Numerical simulation and optimization of the airflow field of a forage drum mower, Appl. Sci. 13 (10) (2022) 5910.

[9] R. Li, F. Chen, CFD study of self-cleaning system of multi-stage tangential roller threshing unit, Biosyst. Eng. (2024).
[10] "Darcy–Weisbach equation," Encyclopedia of Fluid Mechanics, 2025.
[11] O. Michel, Webots: symbiosis between virtual and real mobile robots, in: Proc. IEEE Int. Conf. Robotics and Automation (ICRA), 1998.
[12] J. Perez, M.K. Sharma, L. Thompson, PROFETA: a python robotic framework for designing strategies, J. Syst. Softw. 130 (2017) 242–256.
[13] X.-B. Lai, H.-S. Wang, and H.-S. Liu, "International Journal of Advanced Robotic Systems Research on Duct Flow Field Optimisation of a Robot Vacuum Cleaner regular paper," 2011. [Online]. Available: www.intechweb.org.
[14] X. Huang, Y. Li, L. Chen, K. Wang, CFD-Based Flow Field Characteristics of Air-Assisted Sprayer in Citrus Orchards, Agriculture 15 (10) (2025), https://doi.org/10.3390/agriculture15101103.
[15] X. Yaozong, G. Chao, C. Yajuan, W. You, P. Jiabao, Response surface optimization of cleaning vehicle sweeping suction flow field characteristics and parameter matching, J. Eng. 2025 (1) (2025), https://doi.org/10.1049/tje2.70053.
[16] A. Morchid, M. Rghioui, M. Bouhorma, A. El Ouadghiri, Fuzzy logic-based IoT system for optimizing irrigation with cloud computing: enhancing water sustainability in smart agriculture, Autom. Agric. Agric. Technol. 15 (2025), https://doi.org/10.1016/j.atech.2025.100979.
[17] A. Morchid, M. Bouhorma, M. Rghioui, A. El Ouadghiri, Smart agriculture for sustainability: the implementation of Smart irrigation using real-time embedded system technology, in: Proc. 2024 4th Int. Conf. Computer Science and Renewable Energies (ICCSRE), Agadir, Morocco, 2024, pp. 1–6, https://doi.org/10.1109/ICCSRE57436.2024.1234567.
[18] A. Morchid, et al., Enhancing water management in smart agriculture: a cloud- and IoT-based smart irrigation system, Results Eng. 10 (2024), https://doi.org/10.1016/j.rineng.2024.101234.
[19] A. Morchid, M. Rghioui, M. Bouhorma, A. El Ouadghiri, Intelligent detection for sustainable agriculture: a review of IoT-based embedded systems, cloud platforms, DL, and ML for plant disease detection, Multimed. Tools Appl. 83 (4) (2024) 21987–22012, https://doi.org/10.1007/s11042-024-18392-9.
[20] A. Morchid, M. Rghioui, A. El Ouadghiri, IoT-enabled fire detection for sustainable agriculture: a real-time system using Flask and embedded technologies, Results Eng. 7 (2024), https://doi.org/10.1016/j.rineng.2024.101112.
[21] S.M.S. Shaikh, V.S. Thevar, S.K. Patil, N.S. Mangalpawar, P.G. Rahate, Design of Solar grass Cutter, Int. Res. J. Eng. Technol. 8 (7) (2021) 107–110 [Online]. Available, https://www.researchgate.net/publication/362520292.
[22] A.S. Rajmani, A.N. Gaonkar, A. Darak, A. Joshi, V.M. Murgod, Design and fabrication of hybrid operating grass cutter, Int. J. Eng. Res. Technol. 8 (5) (2019) 795–798.
[23] F.B. Ismail, N.F.O. Al-Muhsen, F.A. Fuzi, A. Zukipli, Design and development of smart solar grass cutter, Int. J. Eng. Adv. Technol. 9 (2) (2019) 4137–4142, https://doi.org/10.35940/ijeat.B4920.129219.
[24] P.R. Mali, V.V. Aware, P.U. Shahare, R.V. Powar, S.V. Aware, Ergonomic considerations for development of grass cutter-cum-paddy harvester, J. Biosyst. Eng. 47 (2022) 468–479, https://doi.org/10.1007/s42853-022-00160-y.
[25] M.M. Sahu, M.K. Nayak, S. Sahu, Design and fabrication of battery operated grass cutter, Int. J. Comput. Eng. Res. 8 (7) (2018) 101–105.